Materials Today Bio 31 (2025) 101521

Contents lists available at ScienceDirect

Materials Today Bio

journal homepage: www.journals.elsevier.com/materials-today-bio

Multifunctional liposome boosts glioma ferroptosis and immunotherapy through reinforcement of chemo-dynamic therapy strategy

Hongwu Chen [a,b], Jiehao Huang [a,b], Huaiming Wang [b], Yimin Xu [b], Jieling Chen [a], Tingting Deng [a], Zhongjing Su [a,**], Rui Lin [b,***], Cong Huang [b,*], Jie Wu [a,****]

[a] Shantou University Medical College, Shantou, 515041, China
[b] The First Affiliated Hospital of Shantou University Medical College, Shantou, 515041, China

ARTICLE INFO

Keywords:
Glioma
Chemo-dynamic therapy
Ferroptosis
Immunotherapy
Liposome

ABSTRACT

Glioma remains significant challenging to completely cure by the conventional surgical resection because of its high infiltrative growth properties. Recently, emerging immunotherapy has achieved remarkable success in treating various cancer, but glioma do not benefit from cancer immunotherapy owing to its specific immunosuppressive tumor microenvironment (iTME). Herein, we show the significant improvement of the immunotherapy efficacy for glioma through multifunctional liposome (Lpo@Cu_2Se-GOx). After tumor cells endocytosis, the released glucose oxidase (GOx) could oxidize glucose into gluconic acid to achieve starvation therapy and generate H_2O_2 as byproduct. Meanwhile, these properties might further cause anti-oxidant systems dysfunction and reinforce Cu^{2+} based Fenton-like reaction, which lead to lipid peroxides accumulation and ferroptosis occur. Moreover, the onset of ferroptosis would trigger the release of damage-associated molecular patterns and induce immunogenic cell death, which contributed to the dendritic cell maturation and cytotoxic T cell infiltration. Besides, in vitro and in vivo experiments verified that Lpo@Cu_2Se-GOx had well significant glioma inhibition without adverse reactions. Taken together, our research demonstrates the modulation of iTME through self-amplified chemo-dynamic therapy could be a significant strategy to improve the immunotherapy of glioma.

1. Introduction

Although break through progress has been achieved in the treatment of malignant tumors in recent year, glioma remains the most common and fatal malignant tumor, with a 5-year survival rate of less than 10 % [1,2]. Owing to the presence of blood-brain barrier (BBB), there is still a lack of effective drugs for the treatment of glioma [3]. Notably, the emerging immunotherapy has been paid more attention in the therapy of glioma [4,5]. With in-depth study, increasing researches confirm that glioma belongs to the "cold tumor" [6,7], which exhibits poor response to immunotherapy; besides, the BBB also serves as a physical barrier to inhibit the infiltration of cytotoxic immune cells. Therefore, how to effectively reshape the immune-suppressed tumor microenvironment is a pivotal issue for breaking through "bottle-neck" of glioma treatment.

Ferroptosis is a novelly discovered programmed cell death pathway [8–10]. In fact, the ferroptosis could be mainly initiated by the accumulated intracellular lipid peroxides. As reported, the Fenton or Fenton-like reaction, triggered by various metal ions (such as, Fe, Cu, Mn, and et al.), could promote reactive oxygen species (ROS) generation and trigger ferroptosis [11–16]. Interestingly, emerging study identified that Cu could directly binds to GPX4 protein, leading to the formation of GPX4 aggregates and subsequent autophagic degradation of GPX4 [17]. Therefore, Cu-based nanoparticles exhibited a more pronounced advantage in inducing ferroptosis. During the process of ferroptosis, the cancer cells could release damage-associated molecular patterns (DAMPs) and further induce immunogenic cell death (ICD), which possesses powerful immunogenicity and exhibits prominently anti-tumor effect [18,19]. For example, Li et al. developed a novel nanoscale metal organic framework, which could boost ferroptosis-mediated immune response through Fenton and Fenton-like reaction [19]. Nevertheless, these ferroptosis-based antitumor therapeutics would be limited in two aspects [20,21]: Firstly, the inadequate

* Corresponding authors.
** Corresponding author.
*** Corresponding authors.
**** Corresponding author.
E-mail addresses: g_zjsu@stu.edu.cn (Z. Su), linrui2009@163.com (R. Lin), chuang200628@163.com (C. Huang), jiewu@stu.edu.cn (J. Wu).

https://doi.org/10.1016/j.mtbio.2025.101521
Received 9 November 2024; Received in revised form 5 January 2025; Accepted 24 January 2025
Available online 27 January 2025

H_2O_2 concentration within tumor microenvironment is not enough to maintain the continuously Fenton reaction; Secondly, the glutathione peroxidase 4 (GPX4) and ferroptosis suppressor protein 1 (FSP1) could promote the detoxification of lipid peroxides [22].

As two key signaling component of ferroptosis inhibited mechanism, GPX4 can react with glutathione (GSH) to degrade the cytotoxic lipid peroxides, while FSP1 can trap the lipid peroxyl radicals with the recycling of coenzyme Q10 (CoQ10) to ubiquinol (CoQ10H2) [23,24]. Actually, the generation of intracellular GSH and CoQ10H2 levels were highly depended on $NADP^+$/NADPH ratio; notably, the NADPH was mainly produced through pentose phosphate pathway (PPP) with the consumption of glucose [25]. Emerging studies identified that glucose oxidase (GOx) could oxidize glucose into nonmetabolizable gluconic acid to achieve starvation therapy, and generate H_2O_2 as byproduct [26,27]. Taken together, the combination of GOx might help to suppress the above anti-ferroptotic pathways and achieve continual Fenton reaction, which contributed to the enhancement of ferroptosis and following anti-tumor immune response.

Among all drug delivery vectors, liposomes, with high biocompatibility and low toxicity, had been proved to be a valuable approach to transport various drugs across BBB [28]. Previous studies found that liposomes can be better absorbed in passive targeted strategy based on the EPR effect, which was attributed to the weakening of the BBB near the glioma [29,30]. Herein, we firstly conjunct Cu_2Se with GOx, and ultimately encapsulated with liposomes to generate Lpo@Cu_2Se-GOx nanoparticles (NPs) for the purpose of ferroptosis-inducing therapy. Upon internalized by the glioma cells, the released GOx would reduce intracellular glucose and increase $NADP^+$/NADPH ratio; meanwhile, the generated H_2O_2 could further strengthen the Cu^{2+}/Cu^+-mediated Fenton-like reaction. Based on that, the intracellular ROS level could be upregulated, and ferroptosis occur (Scheme 1). Overall, Lpo@Cu_2Se--GOx could simultaneously inhibit anti-ferroptotic pathways and

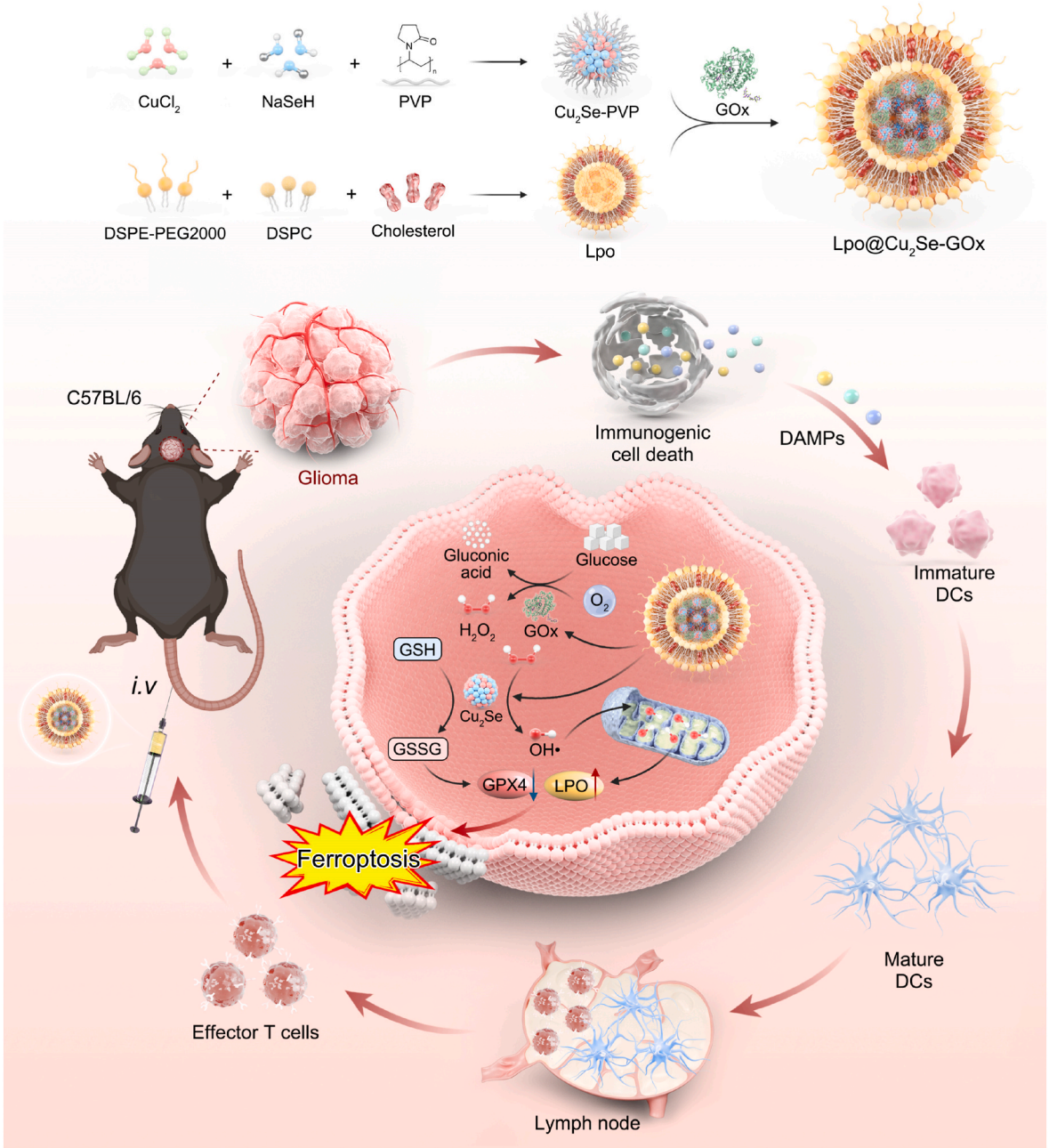

Scheme 1. Schematic illustration of Lpo@Cu_2Se-GOx synthesis with ferroptosis-enhanced immunotherapy mechanism.

promote lipid peroxides accumulation, followed by inducing ferroptosis and ICD, which provided a promising strategy to improve immunotherapy of glioma.

2. Methods

2.1. Synthesis of Cu_2Se NPs

Firstly, 85 mg of $CuCl_2{\cdot}2H_2O$ and 600 mg of PVP (Mw = 8000) were sequentially dissolved. In next step, 39.5 mg of selenium powder was reduced with 56.8 mg of $NaBH_4$, under magnetic stirring, and then added to the copper solution. The solution quickly transformed into a brownish-black solution and then stirred continuously for another 2 h. Following centrifugation at 10,000 rpm, the supernatant was collected and stored at 4 °C for future use.

2.2. Preparation of Cu_2Se-GOx NPs

Firstly, HS-PEG-COOH was used to modify Cu_2Se NPs. In brief, 1 mg of Cu_2Se and 10 mg of HS-PEG-COOH were combined in DI water and subjected to ultrasonication. Following a 24-h PEGylation process, Cu_2Se NPs were PEGylated and obtained. To create the GOx-integrated NPs, GOx and the previously prepared samples were mixed into DI water with 1-ethyl-3-(3-dimethylaminopropyl) carbodiimide hydrochloride (EDC) and continuously agitated for 24 h. The Cu_2Se-GOx NPs were then separated by centrifugation.

2.3. Preparation of Lpo@Cu_2Se-GOx NPs

A mixture of DSPC, cholesterol, and DSPE-PEG-2000 was combined in 5 mL of chloroform in a ratio of 10:1:1. The mixture was dried using rotary evaporation in a round-bottom flask, followed by the addition of a Cu_2Se-GOx solution (1 mg/mL). After 30 min of sonication, the liposome solution was obtained through polycarbonate membranes. After 24 h of dialysis, the resulting purple dispersion of Lpo@Cu_2Se-GOx NPs was collected. This dispersion was then stored at 4 °C and intended for future use within 48 h. Inductively coupled plasma-Mass Spectrometry (ICP-MS) analysis was performed to quantify the concentrations of Cu ions.

2.4. Evaluation of Fenton-like effect

Fenton-like effect was evaluated by detecting the absorbance of MB. Moreover, the absorbance of MB was measured while incubating with Cu_2Se-GOx (40 μg/mL) under varying conditions of H_2O_2 and glucose. These measurements were used to compare the catalytic activities of the NPs and their effectiveness in generating hydroxyl radicals. Additionally, the generation of •OH was measured using electron spin resonance (ESR).

2.5. In vitro H_2O_2 production

The concentration of H_2O_2 produced by Cu_2Se-GOx NPs (40 μg/mL) was quantified using UV–vis absorption spectroscopy. After the reaction, the H_2O_2 levels were estimated by analyzing the UV–vis absorption spectrum according to the standard curve, allowing for accurate quantification of H_2O_2 generation.

2.6. In vitro glucose oxidation reaction

Firstly, Cu_2Se-GOx NPs and GOx were added to the glucose solution. At predetermined intervals, 0.5 mL solution were collected and then, DNS solution was mixed with it. Further, the sample was boiled and then cooled. The glucose concentration over time was determined by recording the UV–vis absorption spectra for each sample.

2.7. GOx release detection

1 mg of nanoparticles were dispersed in 10 mL of PBS with pH values (6.5) and 1 mL of the solution was collected at the time 0 h, 6h, 12h, 24h, 48h, 72h after centrifugation to remove the nanoparticles, the GOx content was determined by using the BCA kit.

2.8. Cu ion release ability

Cu ion release was assessed by a dialysis bag filtration method. Firstly, Lpo@Cu_2Se-GOx NPs was submerged and subjected to continuous shaking with dialysis bag holding. At different intervals, 5 mL samples of PBS were collected to determine the Cu ion concentration. The release ability of Cu ion was then obtained using ICP-MS.

2.9. Cellular internalization of Lpo@Cu_2Se-GOx NPs

The cellular uptake of Lpo@Cu_2Se-GOx NPs was evaluated to understand their internalization efficiency. Cells were incubated with rhodamine-labeled Lpo@Cu_2Se-GOx NPs ([Cu_2Se] = 2 μg/mL) under standard culture conditions. After incubation periods, the cells were washed and further fixed for analysis. Confocal laser scanning microscope (CLSM) or flow cytometry was used to quantify and visualize the internalized NPs, providing insights into the uptake efficiency and distribution within the cells.

2.10. In vitro anti-tumor effect

GL261 cells were seeded and then were treated with different concentrations of Lpo@Cu_2Se and Lpo@Cu_2Se-GOx NPs ([Cu_2Se] = 0, 2, 4, 8, 16, 32, 64 μg/mL). After 24 h co-incubation, the treated cells were collected for the detection of cell viability through CCK-8 assay. Additionally, the proportions of live and dead cells were evaluated by Calcein-AM/PI detection kit.

2.11. Evaluation of the level of ROS

GL261 cells were exposed to either Lpo@Cu_2Se or Lpo@Cu_2Se-GOx ([Cu_2Se] = 16 μg/mL) for a duration of 24 h. Subsequently, the cells were treated with a DCFH-DA probe to measure intracellular ROS levels. Afterwards, the results were captured and analyzed using flow cytometry and CLSM, respectively.

2.12. Evaluation of MMP and mPTP

GL261 cells were treated with Lpo@Cu_2Se or Lpo@Cu_2Se-GOx NPs ([Cu_2Se] = 16 μg/mL). Next, the mitochondrial membrane potential (MMP) was assessed by JC-1 kit. Additionally, alterations in mitochondrial permeability transition pore (mPTP) were examined using a dedicated mPTP detection kit.

2.13. Evaluation of mtROS

Firstly, GL261 cells were treated with either Lpo@Cu_2Se or Lpo@Cu_2Se-GOx NPs ([Cu_2Se] = 16 μg/mL). Following a 24-h period, the levels of mtROS within the cells were assessed using the MitoSOX™ Red indicator (Invitrogen) and subsequently analyzed through flow cytometry.

2.14. Evaluation of intracellular lipid peroxide

GL261 cells were treated with either Lpo@Cu_2Se or Lpo@Cu_2Se-GOx NPs ([Cu_2Se] = 16 μg/mL) for an additional 24 h after seeding in confocal dishes. To visualize lipid peroxidation, the cells were stained with C11-BODIPY 581/591, followed by staining with hochest 33342 to label the nucleus. Finally, the represented images were captured using

CLSM.

Moreover, the malondialdehyde (MDA) concentrations were measured using an MDA assay kit (Solarbio). In brief, the treated cells were collected, lysed and centrifuged to obtain the supernatant. Subsequently, after the addition of MDA assay working solution, the absorbance was measured and recorded for further analysis.

2.15. Assessment of GPX4 activity and GSH level

Firstly, the treated GL261 cells were collected. Then, the changes of intracellular GSH content were detected through commercial GSH assay kit. Besides, the changes of GPX4 activity were evaluated through cellular glutathione peroxidase assay kit.

2.16. Detection of immunogenic cell death biomarkers

GL261 cells were planted in the confocal dishes for 24 h. Afterwards, the cells were treated with various nanocomposites. Afterwards, these cells were fixed, blocked, and incubated with primary rabbit anti-CRT or anti-HMGB1 for 12 h at 4 °C. Subsequently, the cells were stained with Cy3-conjugated goat anti-rabbit IgG antibody, and DAPI, respectively. Finally, the represented images were captured by CLSM. Besides, the treated cells were collected and incubated with PE-labeled anti-CRT antibody, and then detected by flow cytometry assay.

Furthermore, the supernatant from each cell sample after various treatment, were obtained to detect the release of HMGB1 with ELISA kit. Additionally, we also applied chemiluminescence ATP determination to detect the release level of ATP.

2.17. In vitro DC cells maturation detection

Firstly, the GL261 cells were pre-treated with Lpo@Cu_2Se or Lpo@Cu_2Se-GOx NPs ([Cu_2Se] = 16 μg/mL). Subsequently, the GL261 cell supernatants were added and co-incubated with DC cells for another 48 h. Afterwards, these DC cells were collected, and stained with anti-CD86 and anti-CD86 for flow cytometry. An ELISA kit (Meilian Bio Corporation, Shanghai) was used to assay the cytokines (IL-6) released by DC cells in cell culture supernatants.

2.18. In vivo anti-tumor efficacy

All animal procedures were approved by Animal Care and Use Committee of SUMC (SUMCSY2024-011), and all investigation procedures were carried out in accordance with the Helsinki Declaration. To establish the GL261 intracranial orthotopic glioblastoma mouse model, C57BL/6J mice were anesthetized with 2.0 % isoflurane and placed in a stereotactic device. GL261-luc cells (5.0 × 10^5) were injected into the right striatum (coordinates: 2.0 mm lateral to the midline, 0.5 mm anterior to bregma, 3.5 mm depth) using a mouse adaptor. After 9 days, these mice were randomly divided into three groups, including PBS, Lpo@Cu_2Se and Lpo@Cu_2Se-GOx. The concentration of Cu_2Se in both nanocomposites-treated group was 2 mg/kg. During the treatment period, the growth of intracranial glioblastoma cells was monitored via bioluminescence imaging. On day 27, the mice were euthanized, and tumor samples were harvested for further experiments. Additionally, the tumor tissues were harvested, and fixed in 4 % formalin for H&E staining, as well as Ki67, TUNEL, CRT and HMGB1.

2.19. Immune cell assessment

To investigate the immune response triggered by Lpo@Cu_2Se-GOx NPs, tumor tissues and tumor-draining lymph node were obtained from mice in various samples. The tissues were enzymatically digested, and single-cell suspensions were created by filtering and the isolated cells were initially blocked. Next, the cells were labeled with CD3, CD8 and CD45 antibodies to determinate the $CD8^+$ T cell population in tumor tissues using flow cytometry. Besides, the effective $CD8^+$ T cells in the tumors were identified with CD45, CD3, CD8, and GZMB antibodies. Additionally, the frequency of mature DCs in the lymph nodes was examined by flow cytometry after staining with anti-CD45, anti-CD11c, anti-CD80 and anti-CD86. Moreover, the cells were stained with antibodies against anti-CD45, anti-CD4, anti-Foxp3, and anti-CD3 to identify the proportion of Treg cells.

2.20. Hemolysis assessment

Red blood cells were harvested and incubated with varying concentrations of Lpo@Cu_2Se-GOx NPs, ranging from 0 to 200 μg/mL, to assess hemolysis. The hemolysis rate for each group was calculated by measuring the optical density (OD) value with a microplate reader.

2.21. In vivo safety assessment

To assess the in vivo toxicity of Lpo@Cu_2Se-GOx, serum samples from tumor-bearing mice were analyzed for liver function markers (AST, ALT), renal function indicators (CR, BUN), and routine blood tests (WBC, RBC, PLT). Additionally, the heart, liver, spleen, lung, and kidney were harvested from the mice for H&E staining to evaluate any potential tissue damage.

2.22. In vitro BBB-crossing efficiency

To establish the in vitro BBB model, we used the mice brain endothelial bEnd.3 cell. Briefly, we seeded 2 × 10^5 bEnd.3 cells in the transwell upper chamber (0.4 μm pore size) and cultured for about 7 days to reach TEER higher than 200 Ω cm^2. Then we seeded GL261 cells on the bottom chamber and co-incubation for 24 h. Then we added RhB labeled Cu_2Se, Cu_2Se-GOx, Lpo@Cu_2Se and Lpo@Cu_2Se-GOx into the apical chamber and waiting for 4 h. The GL261 cell's nuclei were stained by DAPI for 10 min, and the Fluorescence intensity of cells in the bottom well was observed by CLSM and quantified by flow cytometry.

2.23. In vivo bio-distribution and metabolism study

Firstly, in order to evaluate the in vivo Bio-distribution of Lpo@-Cu_2Se-GOx, the healthy C57BL/6J mice were intravenously injected with Lpo@Cu_2Se and Lpo@Cu_2Se-GOx (2 mg/kg, 150 μL) separately. At the indicated time point (1h, 6h, 12h, 24h, 48h, 72h), the main organs and tumor were collected, weighted and dissolved in digesting aqua regia. The concentrations of Cu ions in different samples were detected by ICP-MS.

2.24. Statistical analysis

The data was presented as the average plus the standard deviation. One-way ANOVA was used to analyze the variations among multiple groups. Statistically significant results were determined for p-values less than 0.05.

3. Result and discussion

3.1. Synthesis and analysis of Lpo@Cu_2Se-GOx NPs

In this study, TEM analysis demonstrated that the synthesized Cu_2Se-PVP NPs possess a consistent spherical shape (Fig. 1A) [31]. Simultaneously, Cu_2Se-GOx NPs were effectively produced via functional group modification. Thereafter, using the thin-film dispersion technique, liposome NPs and Lpo@Cu_2Se-GOx NPs were produced [32]. Fig. 1B and C shows TEM images that demonstrate a distinct membrane layer coating the surface of liposome NPs. It was observed that the particle size of Lpo@Cu_2Se-GOx NPs was slightly larger compared to liposome NPs. Furthermore, elemental mapping images showed that the Cu and Se

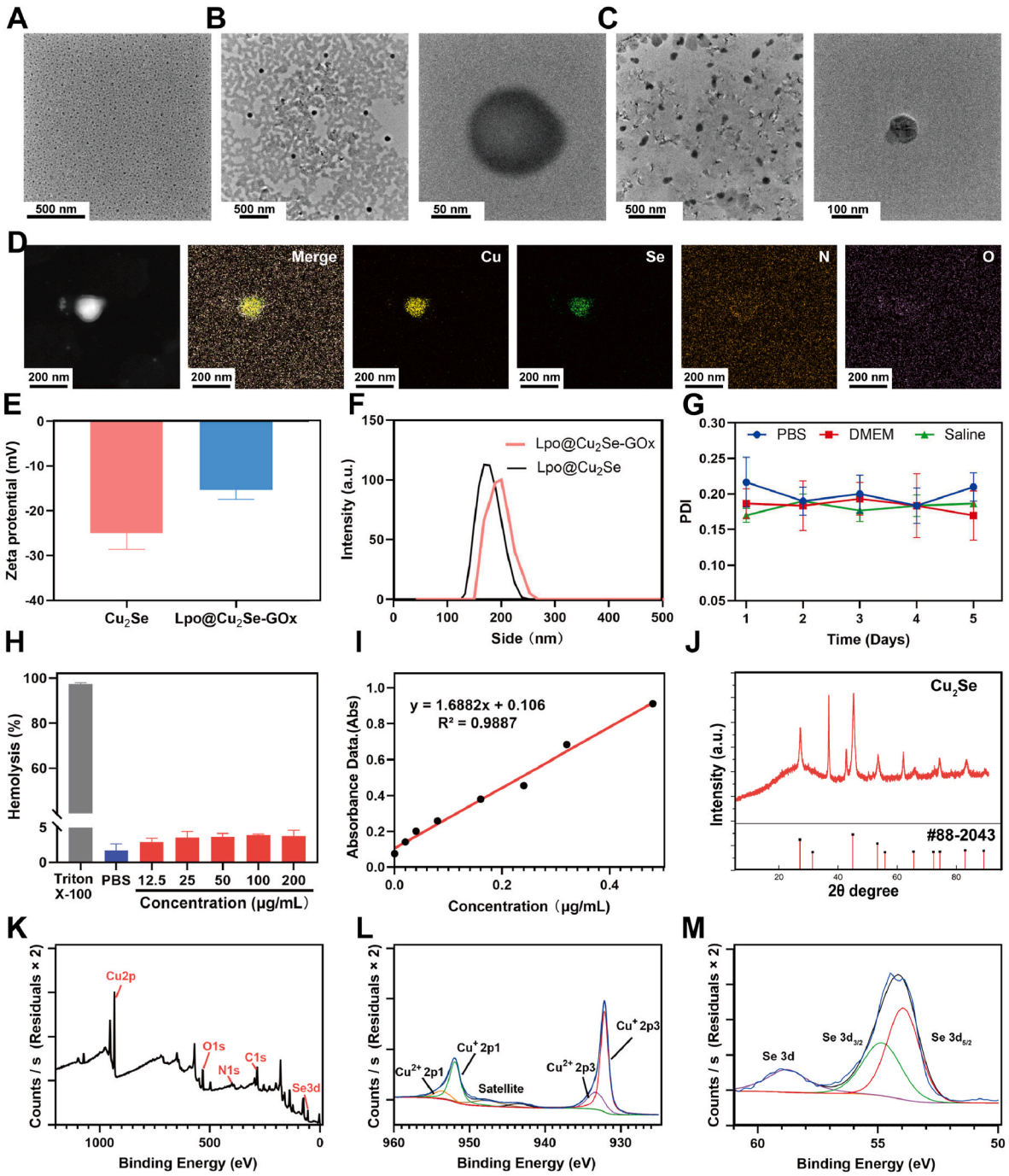

Fig. 1. (A) TEM image of Cu_2Se NPs, scale bar: 500 nm. (B) Low magnification TEM image of liposome NPs, scale bar: 500 nm and high magnification TEM image of liposome NPs, scale bar: 50 nm. (C) Low magnification TEM image of Lpo@Cu_2Se-GOx NPs, scale bar: 500 nm and high magnification TEM image of Lpo@Cu_2Se-GOx NPs, scale bar: 100 nm. (D) HAADF TEM image and elemental mapping of Lpo@Cu_2Se-GOx NPs. (E) Zeta potential of NPs. (F) DLS of Lpo@Cu_2Se and Lpo@Cu_2Se-GOx NPs. (G) PDI of Lpo@Cu_2Se-GOx NPs in different times. (H) Hemolysis test of RBCs in TritonX-100, PBS, and Lpo@Cu_2Se-GOx NPs at various concentrations. (I) The standard curve of GOx based on BCA Protein Assay Kit. (J) XRD patterns of Cu_2Se NPs. (K) XPS of Cu_2Se NPs. (L) High-resolution XPS scans of Cu(2p). (M) High-resolution XPS scans of Se(3d).

elements were evenly dispersed (Fig. 1D) and additionally, the change in zeta potential further confirmed the effective preparation of Lpo@Cu_2-Se-GOx NPs, leading to extended circulation time in the bloodstream and improved durability (Fig. 1E). Dynamic light scattering (DLS) determined that the hydrodynamic size of Lpo@Cu_2Se-GOx NPs was approximately 200 nm (Fig. 1F). Moreover, as depicted in Fig. 1G, the PDI of the Lpo@Cu_2Se-GOx and Lpo@Cu_2Se-GOx NPs remained stable after 5 days in PBS, DMEM and saline, confirming their stability (Fig. S1, Supporting Information). Furthermore, a hemolysis test was conducted to evaluate the biocompatibility of Lpo@Cu_2Se-GOx NPs. Fig. 1H demonstrates that the hemolysis levels were below 5 % across all tested concentrations, indicating that the Lpo@Cu_2Se-GOx NPs are compatible with blood and suitable for prolonged circulation. Using ICP-OES, the encapsulation efficiency (EE%) of Cu_2Se was found to be 58 %. Additionally, the drug-loading rate (DL%) of Cu_2Se in Lpo@Cu_2Se-GOx NPs was approximately 8.4 % and the GOx content was quantified by the BCA Protein Assay Kit, based on the standard curve (Fig. 1I). Moreover, the XRD pattern of the Cu_2Se NPs verified the successful formation of

Cu_2Se crystals (Fig. 1J). The formation of Lpo@Cu_2Se-GOx NPs was further confirmed through XPS (Fig. 1K). In detail, the Cu2p spectrum displayed prominent peaks at 933.46 eV for Cu^+ and 932.19 eV for Cu^{2+} (Fig. 1L). Additionally, Fig. 1M showed the core level spectra of the Se 3d region, the binding energies at 54.8 and 53.9 eV corresponding to Se $3d_{3/2}$ and Se $3d_{5/2}$, respectively, which showed that the valence state of Se in Cu_2Se was −2. Moreover, as shown in Fig. S2 (Supporting Information), the Cu_2Se-GOx shows no change in structural characteristics compared with the native GOx, suggesting that the secondary structure of GOx was well maintained after modification. These results validate the effective formation of Lpo@Cu_2Se-GOx NPs.

3.2. In vitro generation of hydroxyl radicals and H_2O_2

It is well established that the copper ion-catalyzed Fenton reaction can transform H_2O_2 into highly reactive hydroxyl radicals (•OH) [16,19,33,34]. Consequently, we examined whether Lpo@Cu_2Se-GOx NPs could increase the generation of hydroxyl radicals (•OH) using the MB assay. Initially, the capacity to produce •OH radicals was evaluated using the MB assay with different concentrations of H_2O_2. As shown in Fig. 2A, Lpo@Cu_2Se-GOx NPs demonstrated significant •OH generation capability when subjected to elevated levels of H_2O_2. In addition, we investigated whether introducing glucose could allow Cu_2Se-GOx NPs to sustain •OH production.

Fig. 2B shows that with higher glucose concentrations, the absorbance of MB declined, high lighting the exceptional catalytic efficiency of Cu_2Se-GOx NPs. This was further confirmed by electron spin resonance (ESR) measurements (Fig. 2C). Additionally, the Fenton-like effect intensified as the concentration of Cu_2Se or Cu_2Se-GOx NPs increased. This was mainly due to the self-generated hydrogen peroxide initiated by GOx (Fig. 2D and E). GOx is an enzyme that facilitates the conversion of glucose, oxygen (O_2), and DI water into gluconic acid and hydrogen peroxide (H_2O_2). To evaluate the enzymatic function of GOx within the nanoreactors, Cu_2Se-GOx NPs were used to quantify the H_2O_2 generated. Potassium iodide (KI) served as a marker for detecting H_2O_2, with the standard detection curve for H_2O_2 presented in Fig. 2F and G. Significantly, Fig. 2H indicates that with increasing concentrations of Cu_2Se-GOx NPs, the H_2O_2 generation level exceeded 350 μM, substantially higher than that in solid tumors (<100 μM). Furthermore, the ability of the hybrid nanocomposite to catalyze glucose oxidation in an aqueous solution was evaluated using GOx and Cu_2Se-GOx NPs. The DNS reagent kit was used to track the variations in glucose concentration over time. During the incubation period, the glucose concentration in the solution steadily diminished (Fig. 2I). Moreover, as depicted in Fig. 2J, the pH level notably dropped upon glucose addition after treatment of the Cu_2Se-GOx NPs. Additionally, the release profile of GOx was assessed with the BCA protein assay kit, revealing that approximately 90 % of GOx was released within 12 h (Fig. 2K). In summary, these findings consistently indicate that Cu_2Se-GOx NPs can efficiently convert glucose into H_2O_2 and gluconic acid. To investigate the release of Cu^{2+}, the NPs were tested at different pH levels using ICP. As shown in Fig. 2L, less than 20 % of Cu^{2+} was released at pH 7.4 within 72 h, whereas approximately 31 % and 41 % were released at pH 6.0 and pH 5.0, respectively. As previously discussed, incorporating GOx enhanced the Cu^{2+}-mediated chemodynamic therapy (CDT) effect by self-generating H_2O_2 and gluconic acid. Additionally, the acidic environment facilitated further Cu^{2+} release, leading to an effective chemodynamic therapy.

3.3. Cellular uptake and cytotoxicity effect of Lpo@Cu_2Se-GOx

BBB is a major physiological barrier to prevent most therapeutic agents from accessing the brain. Interestingly, emerging studies identified that the liposomes could be easily absorbed through EPR effect,

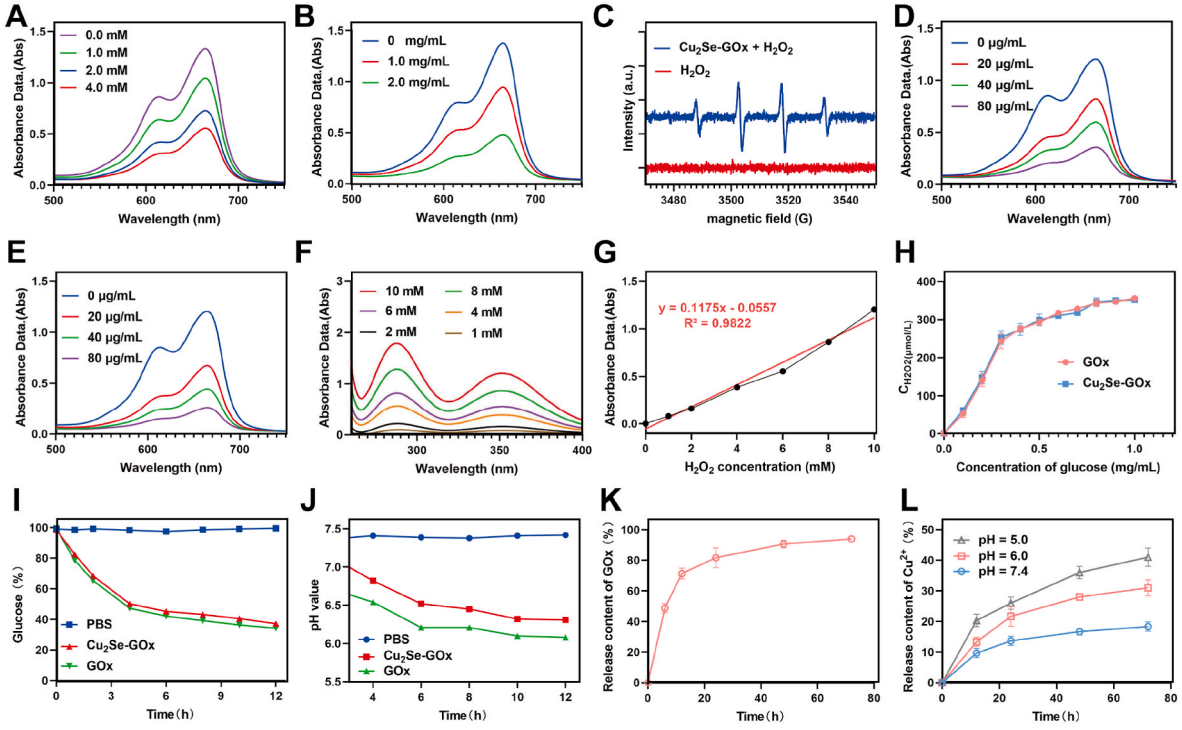

Fig. 2. (A) MB probe degradation with Cu_2Se NPs (40 μg/mL) at varying levels of H_2O_2 (0, 1.0, 2.0, 4.0 mM). (B) MB probe degradation with Cu_2Se-GOx NPs (40 μg/mL) at varying levels of glucose (0, 1.0, 2.0 mg/mL), at concentration of H_2O_2 (2.0 mM). (C) ESR analysis, [H_2O_2] = 2.0 mM, [Cu_2Se-GOx NPs] = 40 μg/mL, pH 6.5. (D) Fenton-like ability of various concentration of Cu_2Se NPs ([H_2O_2] = 2.0 mM). (E) Fenton-like ability of various concentration of Cu_2Se-GOx NPs ([H_2O_2] = 2.0 mM, [Glucose] = 2.0 mg/mL). (F) UV–vis spectra in the KI reaction. (G) The standard curve. (H) H_2O_2 levels after treatment with glucose (1 mg/mL, [Cu_2Se-GOx] = 40 μg/mL). (I) Glucose consumption kinetics. (J) pH levels detection, [Glucose] = 1 mg/mL. (K) The release ability of GOx from the Cu_2Se-GOx NPs (40 μg/mL). (L) The release ability of Cu^{2+} from the Cu_2Se-GOx NPs (40 μg/mL).

which attributed to the weakening of the blood-brain barrier near the glioma [35,36]. To validate its uptake rate, the Rhodamine B (RhB)-labeled Lpo@Cu_2Se-GOx NPs were incubated with GL261 cells. As shown in Fig. 3A, the intracellular RhB fluorescence was significantly increased as the incubation time was prolonged. In particle, GL261 cells showed remarkably red fluorescence after 4h incubation. Meanwhile, the results of flow cytometry assay also showed confirm its high uptake rate (Fig. 3B). Additionally, in order to determine whether Lpo@Cu_2-Se-GOx could across the BBB, we constructed the in vitro BBB model (Fig. S3A, Supporting Information). As showed in Fig. S3B (Supporting Information), compared with Cu_2Se and Cu_2Se-GOx groups, Lpo@Cu_2Se and Lpo@Cu_2Se-GOx exhibited a much stronger fluorescence signal, indicating the importance of Lpo surface modification. Lpo@Cu_2Se-GOx exhibited a fluorescence signal almost as strong as Lpo@Cu_2Se. These results were further confirmed by flow cytometry, which demonstrated that modification of liposomes modification could efficiently promote the penetration of Lpo@Cu_2Se and Lpo@Cu_2Se-GOx through the BBB (Fig. S3, Supporting Information). Afterwards, the in vivo BBB-crossing evaluation was performed with an orthotopic glioma mouse model. Briefly, the orthotopic glioma mouse models were intravenously injected with Cy-5.5 labeled Lpo@Cu_2Se and Lpo@Cu_2Se-GOx NPs, and then the intro-tumor fluorescence intensity were detected by living animal imaging system. As displayed in Fig. 3C, with the prolongation of injection time, a significant increased fluorescence signals were observed within tumor region, peaking at 24h. Taken together, Lpo@Cu_2Se-GOx NPs can penetrate the BBB, which would be a promising treatment strategy for gliomas.

Considering the efficient cellular uptake and CDT properties, we determine the cytotoxicity of Lpo@Cu_2Se-GOx NPs in GL261 cells and normal cells (bEnd.3 cells). bEnd.3 cells showed high cell viability when treated with Lpo@Cu_2Se-GOx at various concentrations, which further confirmed its bio-safety (Fig. S4, Supporting information). Notably, our

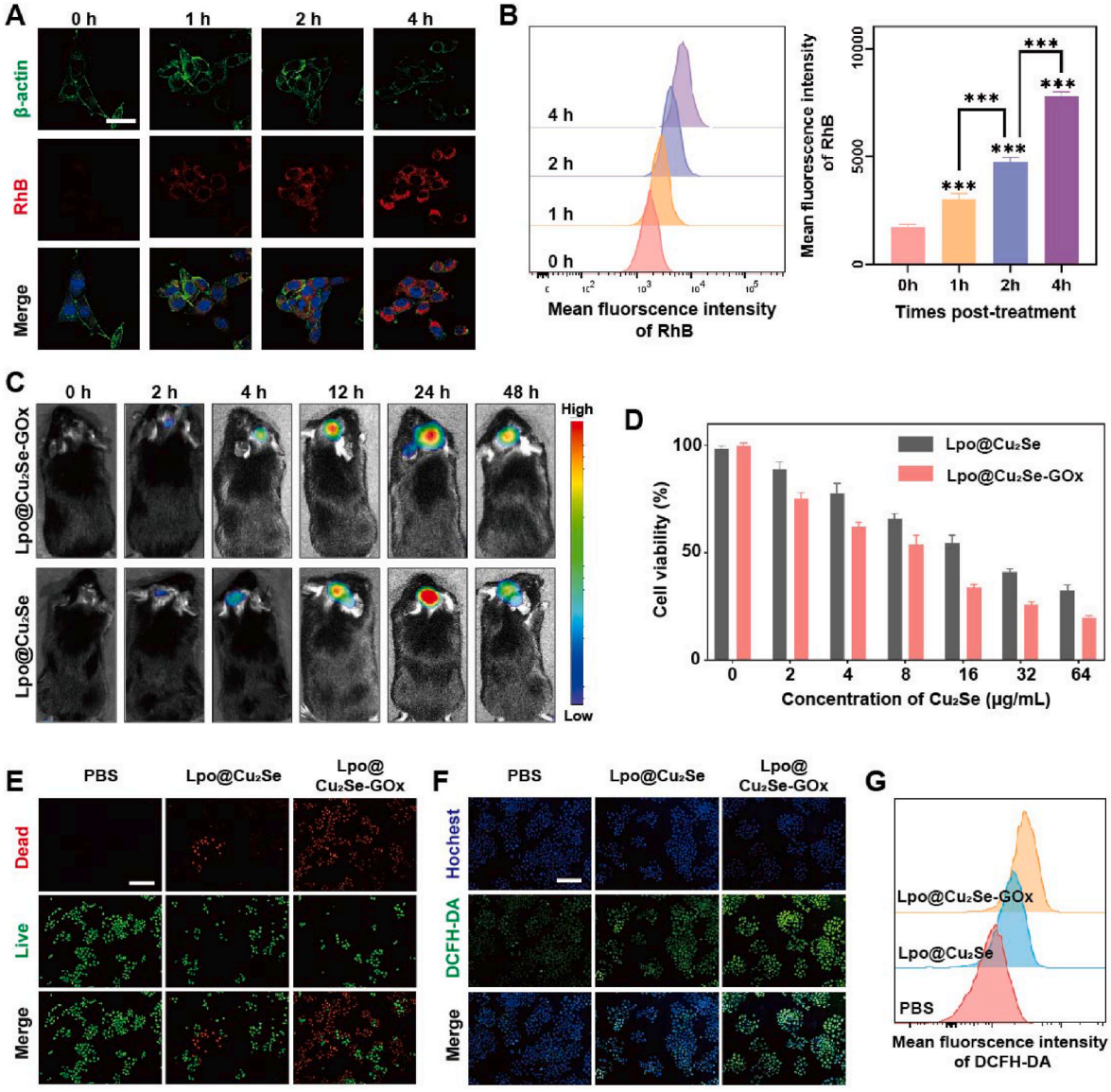

Fig. 3. (A) In vitro fluorescence imaging showed the uptake of RhB-labeled Lpo@Cu_2Se-GOx by GL261 cells at indicated time points, scale bar: 30 μm. (B) Flow cytometry images and statistical analysis for the internalization of RhB-labeled Lpo@Cu_2Se-GOx by GL261 cells. (C) In vivo fluorescence images and statistical analysis of GL261 orthotopic GBM bearing mice at different time points following i.v. injection of Cy5.5-labeled Lpo@Cu_2Se and Lpo@Cu_2Se-GOx NPs. (D) Viability of GL261 cells after treated with Lpo@Cu_2Se and Lpo@Cu_2Se-GOx NPs at different concentration of Cu_2Se. (E) Fluorescence images of GL261 cells stained with calcein AM (green, live cells) and propidium iodide (red, dead cells) after various treatments, scale bar: 100 μm. (F–G) Intracellular ROS level in GL261 cells after various treatments, detected by (F) fluorescent inverted microscopy and (G) flow cytometry assay, scale bar: 100 μm. Data are shown as mean ± SD (n = 3). $^*P < 0.05$, $^{**}P < 0.01$, $^{***}P < 0.001$.

results demonstrated that, within the experimental concentration range of Cu_2Se (0–64 μg/mL), the cell viability showed a remarkable dose-dependent decrease in both Lpo@Cu_2Se and Lpo@Cu_2Se-GOx group (Fig. 3D). However, at the same concentration of Cu_2Se, treatment with Lpo@Cu_2Se-GOx exhibited more stronger cell killing activity, which attributed to the combination of Cu^+/Cu^{2+}-mediated CDT effect and GOx-catalyzed H_2O_2 generation. Meanwhile, we further performed calcein AM (green fluorescence, a signal for live cells) and propidium iodide (red fluorescence, a signal for dead cells) co-staining assay to evaluate its therapeutic effect. As shown in Fig. 3E, compared with Lpo@Cu_2Se group, more red cells and fewer green cells were observed in Lpo@Cu_2Se-GOx group, indicating that Lpo@Cu_2Se-GOx had a higher toxicity to GL261 cells (Fig. S5, Supporting Information).

In order to clarify the therapeutic mechanism triggered by Lpo@Cu_2Se-GOx, we further detect the intracellular ROS generation levels. In fact, previous studies identified that the Fenton-like activity was highly

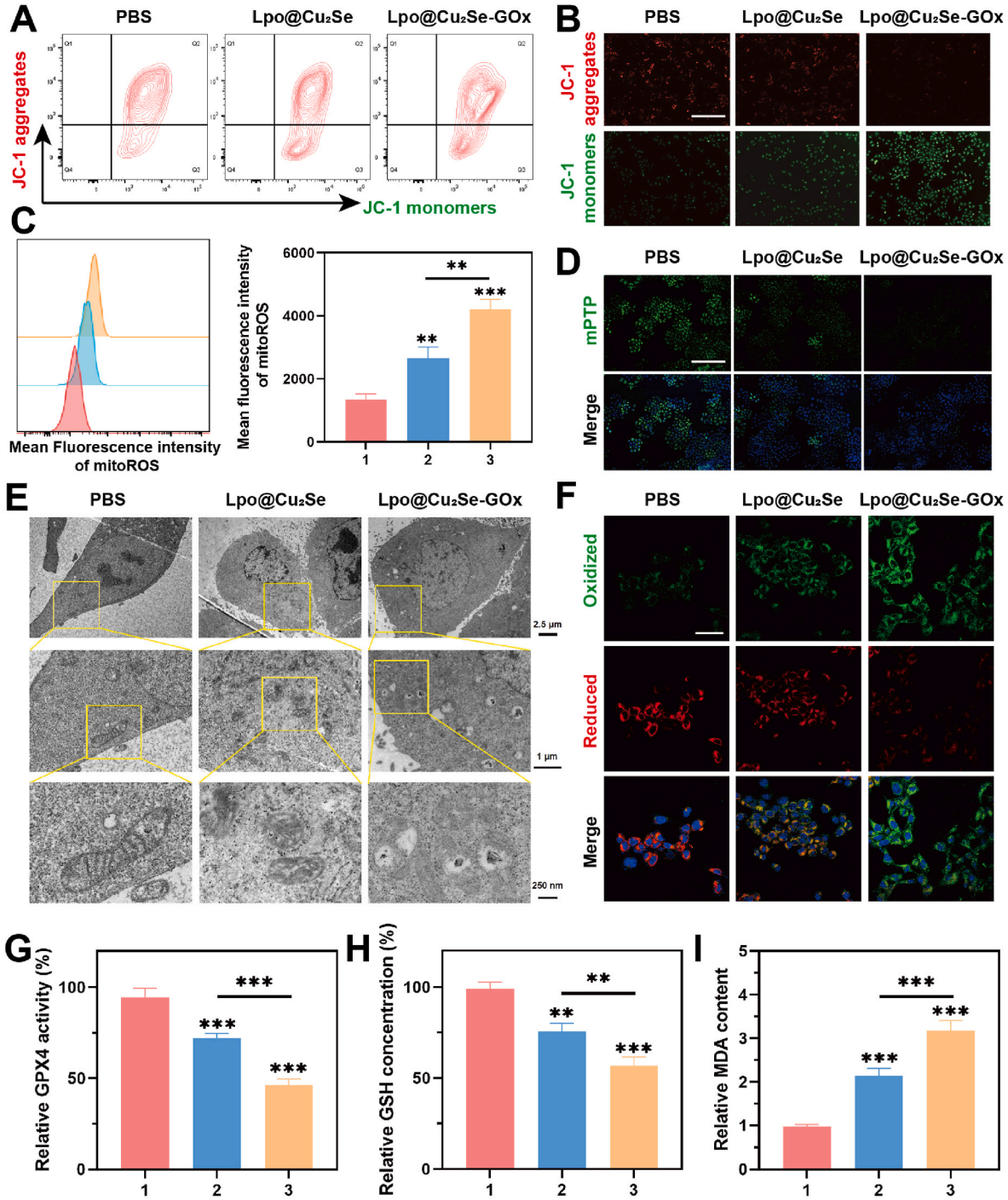

Fig. 4. (A) Flow cytometry analysis of the changes of mitochondrial membrane potential after various treatments. (B) CLSM detection of the changes of mitochondrial membrane potential, scale bar: 100 μm. (C) Flow cytometry images and relative statistical analysis of mitoROS inside treated cells. (D) The open level of mPTP after different treatments, scale bar: 100 μm. (E) TEM observations on the morphological changes of tumor mitochondria with various treatments after 24h post-treatment. (F) LPO assay of GL261 cells using C11-BODIPY 581/591 as probe after different treatments, scale bar: 30 μm. (G–I) Relative (G) GPX4 activity, (H) GSH concentration and (I) MDA content inside GL261 cells treated with different nanoparticles. Group 1: PBS, Group 2: Lpo@Cu_2Se, and Group 3: Lpo@Cu_2Se-GOx. Data are shown as mean ± SD (n = 3). *$P < 0.05$, **$P < 0.01$, ***$P < 0.001$.

depended on the intracellular concentration of H_2O_2, while the addition of GOx could catalyze the oxidation glucose with concomitant production of H_2O_2 [37,38]. Notably, much more conspicuous ROS fluorescence signals were observed in Lpo@Cu_2Se-GOx, when compared to Lpo@Cu_2Se and PBS group (Fig. 3F). Meanwhile, the results of flow cytometry assay also showed the same tendency (Fig. 3G; Fig. S6, Supporting information). In short, we concluded that Lpo@Cu_2Se-GOx could induce oxidative stress of GL261 cells, and finally display enhanced anti-tumor effect.

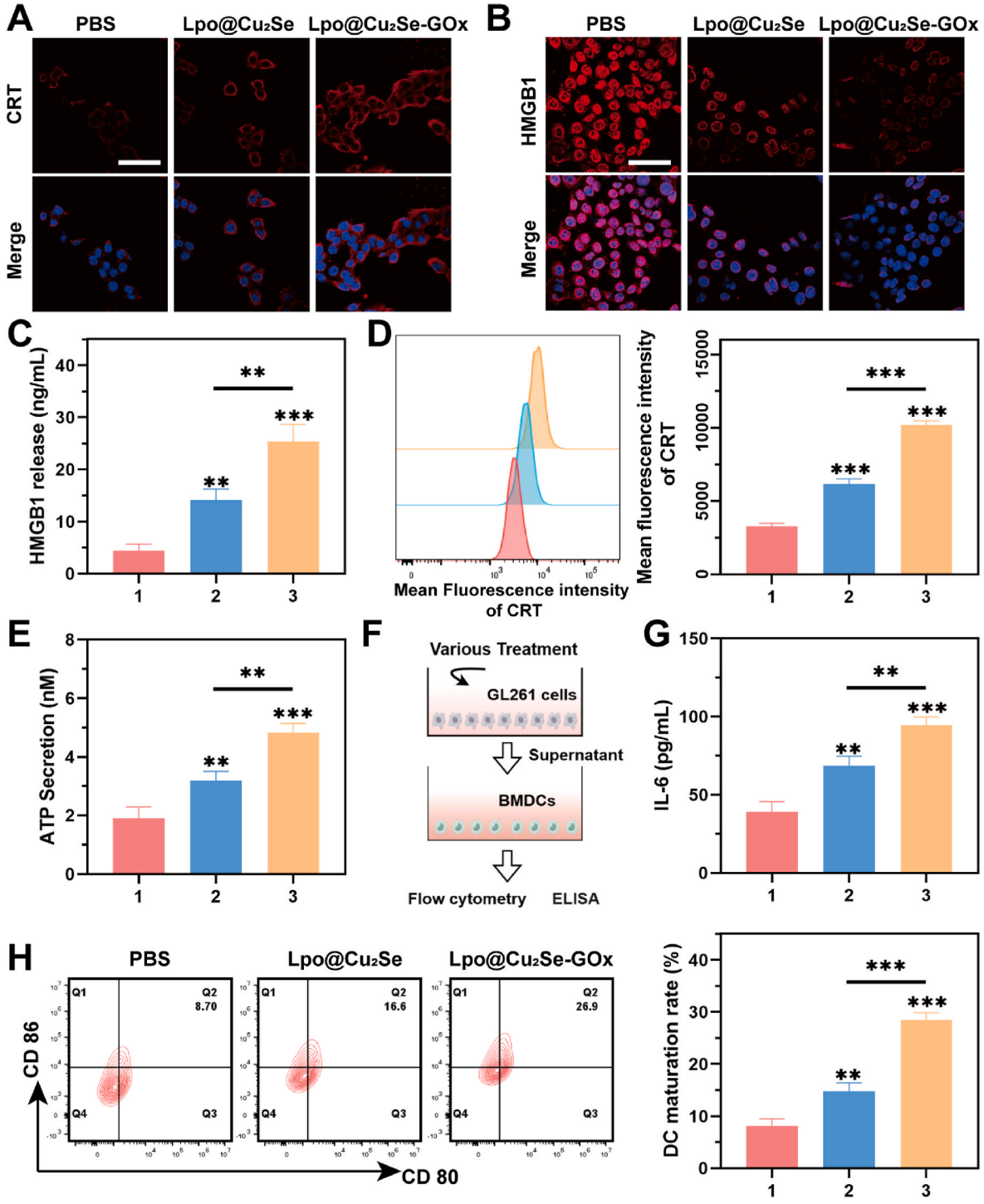

Fig. 5. (A) CLSM images of CRT expression on the GL261 cell surface after being treated with Lpo@Cu_2Se-GOx, scale bar: 30 μm. (B–C) HMGB1 release from GL261 cells treated with different nanocomposites, detected by CLSM and enzyme-linked immunosorbent assay (ELISA) kit, scale bar: 30 μm. (D) Flow cytometry quantification of CRT on surface of GL261 cells. (E) ATP secretion detected by an enhanced ATP assay kit. (F) Schematic illustration of the transwell system showing the design of the DC maturation experiment in vitro. GC261 cells were cocultured in the upper chamber, while DCs cells were cultured in the lower chamber. (G) Statistical chart of IL-6 in co-culture supernatant secreted by DCs. (H) Flow cytometry images showing the mature DCs after different treatments in co-culture system. Group 1: PBS, Group 2: Lpo@Cu_2Se, and Group 3: Lpo@Cu_2Se-GOx. Data are shown as mean ± SD (n = 3). $^*P < 0.05$, $^{**}P < 0.01$, $^{***}P < 0.001$.

3.4. Ferroptosis-inducing capability of Lpo@Cu_2Se-GOx NPs

As we all known, mitochondria are organelles that are susceptible to oxidative stress [39,40]. Herein, in order to determine whether Lpo@Cu_2Se-GOx NPs could impair the mitochondrial function, we firstly detected the changes of mitochondrial membrane potential with JC-1 kit. As shown by the flow cytometry detection results, compared with the PBS and Lpo@Cu_2Se group, the mitochondrial membrane potential in Lpo@Cu_2Se-GOx group was significantly decreased (Fig. 4A; Fig. S7, Supporting Information). Similarly, the CLSM results also exhibited the same tendency, indicating the severe mitochondrial damage triggered by Lpo@Cu_2Se-GOx (Fig. 4B). In addition, the MitoSOX probe was performed to detect the generation of mitochondrial ROS (mitoROS), and the results displayed that Lpo@Cu_2Se-GOx NPs could induce the intracellular mitoROS burst-release (Fig. 4C). Furthermore, our results also revealed that Lpo@Cu_2Se-GOx NPs could force the mitochondrial permeability transition pore (mPTP) to remain open, which is the main reason for the loss of mitochondrial membrane potential (Fig. 4D). Taken together, these findings suggested that Lpo@Cu_2Se-GOx NPs could directly induce mitochondrial dysfunction, leading to a rapid release of mitoROS.

Afterwards, the ferroptosis caused by burst-release of ROS was further evaluated. It is well known that, different from apoptosis, ferroptosis can cause the mitochondria within the cell to shrink [41]. As shown in Fig. 4E, the Lpo@Cu_2Se and Lpo@Cu_2Se-GOx treatment can reduce mitochondrial volume and increase mitochondrial membrane density, which indicated that these nanocomposites can facilitate ferroptosis of GL261 cells. Additionally, we further applied BODIPY581/591-C11 probe to detect the intracellular LPO levels, which is an important indicator of ferroptosis. The result of CLSM showed that highest green fluorescence could be observed in Lpo@Cu_2Se-GOx treatment group, which was attributed to the combination therapeutic effect of CDT effect and GOx-mediated starvation (Fig. 4F). Moreover, emerging studies identified that the addition of GOx would interfere the intracellular NADPH generation through inhibiting PPP pathway [42], while NADPH is essentially required for the generation of GSH. Notably, NADPH/GSH is the major component of cellular anti-oxidant defense system, which dysfunction would promote the intracellular LPO accumulation. As displayed in Fig. 4G–I, our results demonstrated a reduction in GSH and GPX4 activity, accompanied with the markedly increasement of LPO degradation products (such as malondialdehyde (MDA)). Taken together, these results consistently revealed that Lpo@Cu_2Se-GOx NPs could efficiently induce mitochondrial dysfunction and ferroptosis in GL261 cells.

3.5. In vitro immunogenic cell death (ICD) induced by Lpo@Cu_2Se-GOx treatment

Increasing studies reported that the cancer cells underwent ferroptosis, would release immunogenic DMAPs and trigger ICD effect, and finally initiate anti-tumor immune response [43,44]. Actually, the induced ICD was characterized by high mobility group box 1 (HMGB1) release and calreticulin (CRT) exposure, as well as adenosine triphosphate (ATP) secretion. As displayed by CLSM, a highest expression of CRT on the surface of GL261 cells was observed in Lpo@Cu_2Se-GOx group (Fig. 5A). Meanwhile, the results of flow cytometry analysis identified that the intracellular CRT level in Lpo@Cu_2Se-GOx group was higher than that in Lpo@Cu_2Se group (Fig. 5D). As shown in Fig. 5B, a slight weak red fluorescence within GL261 cells was found in Lpo@Cu_2Se-GOx group, indicating that this combination therapeutic effect could promote extracellular efflux of HMGB1 protein. Moreover, the HMGB1 release (Fig. 5C) and ATP secretion (Fig. 5E) was also greatly enhanced by the Lpo@Cu_2Se-GOx, as evaluated by enzyme-linked immunosorbent assay (ELISA) and bioluminescence assay, respectively. Collectively, the above results verified Lpo@Cu_2Se-GOx NPs could induce effective ICD in vitro.

In consideration to the DAMPs can act as a "eat me signal" to promote antigen presentation and DC maturations [45,46], we performed Transwell co-incubated system to determine whether Lpo@Cu_2Se-GOx NPs could make the DC maturations (Fig. 5F). As shown in Fig. 5H, the Lpo@Cu_2Se-GOx increased the maturity of DCs ($CD86^+/CD80^+$ cells) to ~26.9 %, much higher than that in PBS group (~8.7 %) and Lpo@Cu_2Se treated groups (~16.8 %). Besides, we further performed ELISA assay to detect the secretion of IL-6 by matured DCs, which participated in the activation of T cells. Compared with the PBS group, DCs in both Lpo@Cu_2Se and Lpo@Cu_2Se-GOx group have remarkable secretion levels of IL-6 (Fig. 5G). Taken together, the tumor associated antigens derived from ferroptosis cells which triggered by Lpo@Cu_2Se-GOx NPs, could efficiently promote DCs maturation.

3.6. In vivo theragnostic and immune-activated effects of Lpo@Cu_2Se-GOx NPs on orthotopic glioma model

Prior to the therapy, the bio-safety of Lpo@Cu_2Se-GOx NPs was first evaluated through analyzing blood biochemistry. As displayed in Fig. S8 (Supporting Information), compared with PBS group, negligibly small variations in routine blood tests (white blood cells (WBC), red blood cells (RBC), platelets (PLT)) and serum biochemical analysis (alanine aminotransferase (ALT), aspartate aminotransferase (AST), blood urea nitrogen (BUN), creatinine (CREA)) also indicated that the Lpo@Cu_2Se-GOx exhibited excellent bio-safety. Additionally, the H&E staining of major organs showed no significant difference from the group treated with PBS (Fig. S9, Supporting Information). Moreover, to detect the biodistribution results, the Cu content in major organs and tumors were measured at various time points via inductively coupled plasma mass spectrometry after the intravenous injection of Lpo@Cu_2Se-GOx and Lpo@Cu_2Se NPs. As demonstrated in Fig. S10 (Supporting Information), the intravenously injected Lpo@Cu_2Se-GOx and Lpo@Cu_2Se NPs were taken up predominantly by liver and tumor and gradually cleared from the liver and kidney within three days. These results indicated that both Lpo@Cu_2Se-GOx and Lpo@Cu_2Se NPs could be accumulated in tumor tissue and excreted from the body safely, which do not interfere with the metal metabolism of the host animal.Thus, we can conclude that Lpo@Cu_2Se-GOx is a safe therapy with negligible toxicity and good hemocompatibility.

The superior anticancer property Lpo@Cu_2Se-GOx in vitro encouraged us to further investigate its therapeutic efficacy in orthotopic glioma mouse model according to the predesigned protocol (Fig. 6A). On day 9, 15, 21, and 27, three-divided groups of GL261 cells-Luc-bearing orthotopic glioma model mice were treated, and the tumor size was detected by Luc-bioluminescence. Compared to the PBS group, Lpo@Cu_2Se group exhibited a moderate inhibition efficiency within the observation period (Fig. 6B and D). In a significant contrast, Lpo@Cu_2Se-GOx markedly inhibited the growth of orthotopic glioma tumor, largely attributable to GOx-mediated starvation therapy and H_2O_2 self-applied ability (Fig. 6C and D). Meanwhile, Lpo@Cu_2Se-GOx treated mice displayed negligible body weight change, whereas PBS treated mice exhibited significant body weight loss (Fig. 6B). This phenomenal were likely attributed to brain malfunction induced by proliferation and invasion of glioma.

Moreover, as shown in Fig. 6E, the H&E staining slices of brains from three different groups of mice also illustrated that the mouse tumor from the Lpo@Cu_2Se-GOx group was the smallest among the three groups. To further demonstrate the ability of Lpo@Cu_2Se-GOx NPs to kill the cancer cells at tumor site, the Ki-67 staining and terminal deoxynucleotidyl transferase dUTP nick-end labeling (TUNEL) analysis were performed. The weaker red fluorescence in Ki-67 staining, and a stronger red fluorescence in TUNEL analysis could be observed in Lpo@Cu_2Se-GOx treatment group, which further confirmed that this combination therapy could effectively inhibit tumor proliferation and promote cancer cells death (Fig. 6E). Besides, as showed in Fig. S11 (Supporting Information), immunofluorescence-stained tumor sections also showed that treatment

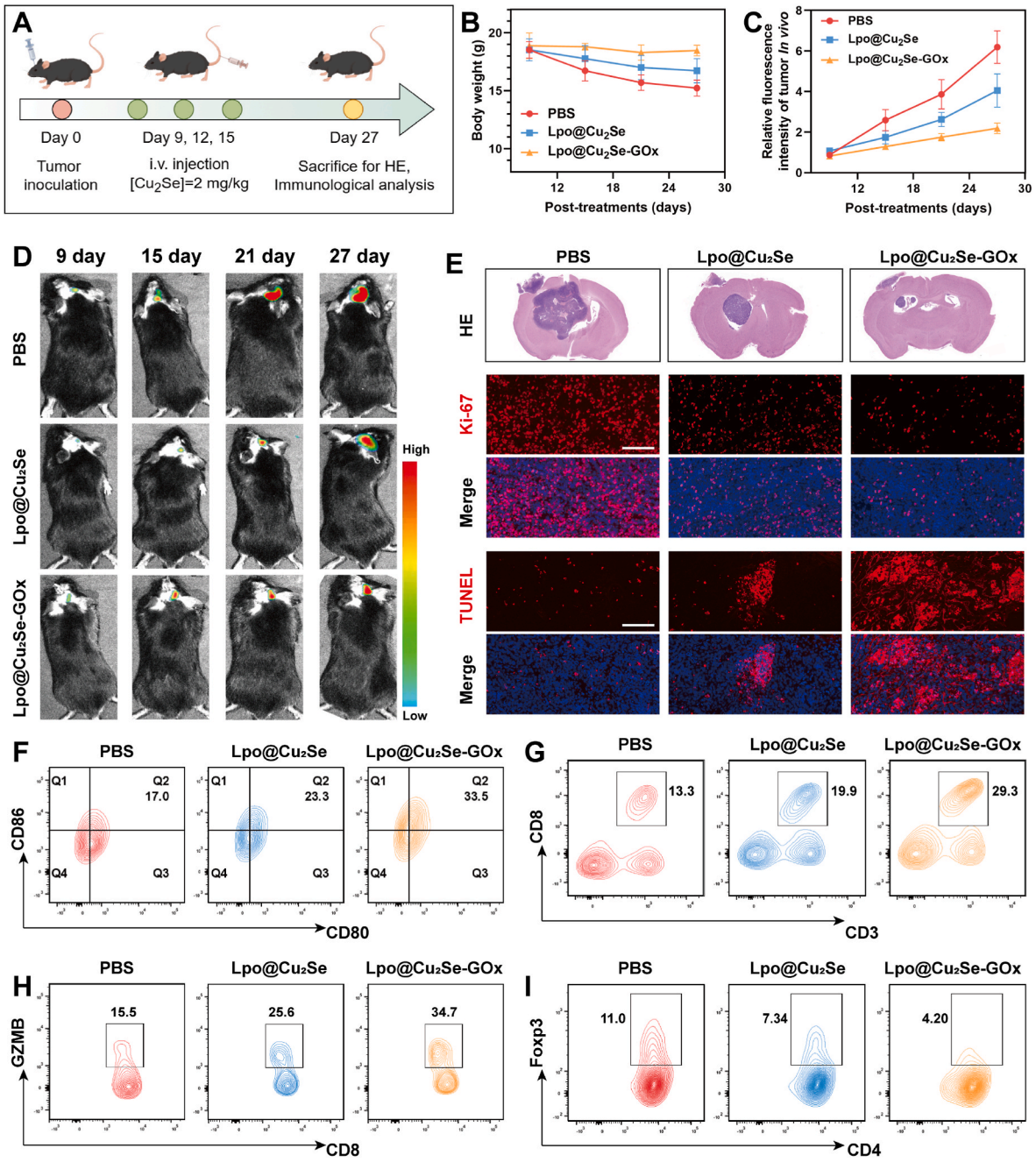

Fig. 6. (A) Schematic illustration of the experimental design. (B) The body weight change of GL261 glioma-bearing mice after different treatments. (C&D) Representative bioluminescence assay images and quantified signal intensity after treated with Lpo@Cu₂Se-GOx, as determined by the living animal imaging system. (E) Representative H&E, Ki67, and TUNEL staining of tumor slices in different groups, scale bar: 100 μm. (F) Representative flow cytometry images of matured DC cells ($CD45^+CD11c^+CD80^+$ $CD86^+$) in tumor-draining lymph nodes. (G–I) Flow cytometry analysis of (G) $CD8^+$ T cells ($CD45^+CD3^+CD8^+$), (H) granzyme B-positive $CD8^+$ T cells, and Treg cells ($CD45^+CD3^+CD4^+CD25^+Foxp3^+$) within post-resection glioma-bearing brain tissues. Data are shown as mean ± SD (n = 4). $^*P < 0.05$, $^{**}P < 0.01$, $^{***}P < 0.001$.

with Lpo@Cu_2Se-GOx could significantly promote CRT expression and HMGB1 secretion, which induce ICD occur and activate anti-tumor immune response.

Furthermore, the effect of anti-tumor immune response was also evaluated by analyzing maturation rate of DCs, as well as the infiltration profiles of both $CD8^+$ T cells and immunosuppressive Tregs cells within tumor. Firstly, the matured DC cells ($CD86^+CD80^+$) in the lymph nodes of neck from three groups of mice are shown in Fig. 6F, in which about 17.0 % of matured DC cells were found in the Lpo@Cu₂Se-GOx group, and they are almost 2- and 1.4-fold higher than those from the Control group and the Lpo@Cu₂Se group, respectively (Fig. S12, Supporting Information). Additionally, the flow cytometry analysis in Fig. 6G displayed that highest $CD8^+$ T cells had been infiltrated into the tumor in Lpo@Cu₂Se-GOx group, which was almost 2.2-fold higher than that in PBS group (Fig. S13, Supporting Information). Meanwhile, these $CD8^+$ T cells showed a high percentage of granzyme B $(GZMB)^+$ (Fig. 6H; Fig. S14, Supporting Information), further verifying the activation of $CD8^+$ T cells. Additionally, the immunosuppressive Treg cells were also detected and showed in Fig. 6I. There was 11.0 % of Treg cells within tumor of mice treated with PBS, but the Treg cells were decreased to 4.20 % after treated with Lpo@Cu₂Se-GOx NPs (Fig. S15, Supporting Information). Taken together, these results identified that Lpo@Cu₂Se-

GOx could initiate immune response and exhibit excellent anti-tumor effect.

4. Conclusion

In this study, we demonstrated a remarkable improvement of glioma immuno-therapy by the reinforcement of chemo-dynamic therapy combined with starvation therapy strategy via multifunctional liposome (Lpo@Cu_2Se-GOx). Upon internalized by glioma cells, Lpo@Cu_2Se-GOx NPs could achieve self-supplied H_2O_2 through glucose oxidization, followed by generate large amounts of ROS through Cu^{2+}-based Fenton-like reaction. Meanwhile, this burst release of ROS might further initiate glioma cells ferroptosis, and induce ICD response, which led to drastically enhanced glioma immunotherapy. This work revealed that our designed Lpo@Cu_2Se-GOx NPs could remodel iTME and exhibit excellent anti-tumor effect. Taken together, we believe that the multi-functional liposome in this study may provide a new insight for tumor immunotherapy, which showing tremendous potential utility in clinical treatment of glioma.

CRediT authorship contribution statement

Hongwu Chen: Writing – original draft, Supervision, Software, Investigation, Data curation, Conceptualization. **Jiehao Huang:** Writing – original draft, Software, Resources, Project administration, Data curation. **Huaiming Wang:** Writing – original draft, Visualization, Investigation, Formal analysis, Data curation. **Yimin Xu:** Resources, Project administration, Methodology, Data curation. **Jieling Chen:** Software, Resources, Project administration, Methodology, Investigation, Funding acquisition. **Tingting Deng:** Writing – original draft, Visualization, Resources, Project administration, Methodology, Funding acquisition. **Zhongjing Su:** Writing – original draft, Visualization, Resources, Project administration. **Rui Lin:** Resources, Methodology, Funding acquisition, Formal analysis. **Cong Huang:** Writing – review & editing, Supervision, Methodology, Conceptualization. **Jie Wu:** Software, Resources, Project administration, Methodology, Conceptualization.

Declaration of competing interest

The authors declare that they have no known competing financial interests or personal relationships that could have appeared to influence the work reported in this paper.

Acknowledgements

This work was supported by grants from the Guangdong Basic and Applied Basic Research Foundation (Grant number: 2023A1515220192), the Medical Scientific Research Foundation of Guangdong Province (Grant number: A2022207, A2024042), the Talented Person Support Plan from The First Affiliated Hospital of Shantou University Medical College (Grant number: YCTJ-2022-09, YCTJ-2023-02).

Appendix A. Supplementary data

Supplementary data to this article can be found online at https://doi.org/10.1016/j.mtbio.2025.101521.

Data availability

Data will be made available on request.

References

[1] J. Kong, R. Zou, G.L. Law, Y. Wang, Biomimetic multifunctional persistent luminescence nanoprobes for long-term near-infrared imaging and therapy of cerebral and cerebellar gliomas, Sci. Adv. 8 (10) (2022) eabm7077.
[2] J. Zhang, L. Han, H. Wu, Y. Zhong, P. Shangguan, Y. Liu, et al., A brain-targeting NIR-II ferroptosis system: effective visualization and oncotherapy for orthotopic glioblastoma, Adv. Sci. 10 (13) (2023) e2206333.
[3] C.D. Arvanitis, G.B. Ferraro, R.K. Jain, The blood-brain barrier and blood-tumour barrier in brain tumours and metastases, Nat. Rev. Cancer 20 (1) (2020) 26–41.
[4] S. Xu, L. Tang, X. Li, F. Fan, Z. Liu, Immunotherapy for glioma: current management and future application, Cancer Lett. 476 (2020) 1–12.
[5] H. Wang, T. Xu, Q. Huang, W. Jin, J. Chen, Immunotherapy for malignant glioma: current status and future directions, Trends Pharmacol. Sci. 41 (2) (2020) 123–138.
[6] T. Wang, H. Zhang, W. Qiu, Y. Han, H. Liu, Z. Li, Biomimetic nanoparticles directly remodel immunosuppressive microenvironment for boosting glioblastoma immunotherapy, Bioact. Mater. 16 (2022) 418–432.
[7] C.M. Jackson, J. Choi, M. Lim, Mechanisms of immunotherapy resistance: lessons from glioblastoma, Nat. Immunol. 20 (9) (2019) 1100–1109.
[8] X. Jiang, B.R. Stockwell, M. Conrad, Ferroptosis: mechanisms, biology and role in disease, Nat. Rev. Mol. Cell Biol. 22 (4) (2021) 266–282.
[9] X. Chen, R. Kang, G. Kroemer, D. Tang, Broadening horizons: the role of ferroptosis in cancer, Nat. Rev. Clin. Oncol. 18 (5) (2021) 280–296.
[10] L. Huang, J. Zhu, G. Wu, W. Xiong, J. Feng, C. Yan, et al., A strategy of "adding fuel to the flames" enables a self-accelerating cycle of ferroptosis-cuproptosis for potent antitumor therapy, Biomaterials 311 (2024) 122701.
[11] X. Lin, H. Chen, T. Deng, B. Cai, Y. Xia, L. Xie, et al., Improved immune response for colorectal cancer therapy triggered by multifunctional nanocomposites with self-amplifying antitumor ferroptosis, ACS Appl. Mater. Interfaces 16 (11) (2024) 13481–13495.
[12] Z. Chen, Z. Li, C. Li, H. Huang, Y. Ren, Z. Li, et al., Manganese-containing polydopamine nanoparticles as theranostic agents for magnetic resonance imaging and photothermal/chemodynamic combined ferroptosis therapy treating gastric cancer, Drug Deliv. 29 (1) (2022) 1201–1211.
[13] Z. Liu, S. Liu, B. Liu, Y. Bian, M. Yuan, C. Yang, et al., Fe(III)-Naphthazarin metal-phenolic networks for glutathione-depleting enhanced ferroptosis-apoptosis combined cancer therapy, Small 19 (19) (2023) e2207825.
[14] L. Huang, J. Zhu, W. Xiong, J. Feng, J. Yang, X. Lu, et al., Tumor-generated reactive oxygen species storm for high-performance ferroptosis therapy, ACS Nano 17 (12) (2023) 11492–11506.
[15] Q. Fan, W. Xiong, H. Zhou, J. Yang, J. Feng, Z. Li, et al., An AND logic gate for magnetic-resonance-imaging-guided ferroptosis therapy of tumors, Adv. Mater. 35 (45) (2023) e2305932.
[16] J. Yang, J. Zhu, B. Ren, H. Cai, Z. Li, Q. Fan, et al., A hollow mesoporous iron oxide nanoparticle to strengthen Fenton reaction and weaken antioxidant defense systems for high efficacy tumor ferroptosis therapy, Chem. Eng. J. 497 (2024) 154470.
[17] Q. Xue, D. Yan, X. Chen, X. Li, R. Kang, D.J. Klionsky, et al., Copper-dependent autophagic degradation of GPX4 drives ferroptosis, Autophagy 19 (7) (2023) 1982–1996.
[18] J. Yang, S. Ma, R. Xu, Y. Wei, J. Zhang, T. Zuo, et al., Smart biomimetic metal organic frameworks based on ROS-ferroptosis-glycolysis regulation for enhanced tumor chemo-immunotherapy, J. Contr. Release 334 (2021) 21–33.
[19] Z. Li, S. He, L. Xie, G. Zeng, J. Huang, H. Wang, et al., Boosting ferroptosis and immunotherapy for colorectal cancer by lactate-related metabolic reprogramming, Adv. Funct. Mater. (n/a) (2024) 2411247 n/a.
[20] J. Lu, Y. Yang, Q. Xu, Y. Lin, S. Feng, Y. Mao, et al., Recent advances in multi-configurable nanomaterials for improved chemodynamic therapy, Coord. Chem. Rev. 474 (2023) 214861.
[21] H. Cheng, Y. He, J. Lu, Z. Yan, L. Song, Y. Mao, et al., Degradable iron-rich mesoporous dopamine as a dual-glutathione depletion nanoplatform for photothermal-enhanced ferroptosis and chemodynamic therapy, J. Colloid Interface Sci. 639 (2023) 249–262.
[22] G. Lei, L. Zhuang, B. Gan, Targeting ferroptosis as a vulnerability in cancer, Nat. Rev. Cancer 22 (7) (2022) 381–396.
[23] K. Bersuker, J.M. Hendricks, Z. Li, L. Magtanong, B. Ford, P.H. Tang, et al., The CoQ oxidoreductase FSP1 acts parallel to GPX4 to inhibit ferroptosis, Nature 575 (7784) (2019) 688–692.
[24] Y. Liu, S. Lu, L.L. Wu, L. Yang, L. Yang, J. Wang, The diversified role of mitochondria in ferroptosis in cancer, Cell Death Dis. 14 (8) (2023) 519.
[25] K. Li, C. Lin, M. Li, K. Xu, Y. He, Y. Mao, et al., Multienzyme-like reactivity cooperatively impairs glutathione peroxidase 4 and ferroptosis suppressor protein 1 pathways in triple-negative breast cancer for sensitized ferroptosis therapy, ACS Nano 16 (2) (2022) 2381–2398.
[26] Y. Ge, F. Rong, Y. Lu, Z. Wang, J. Liu, F. Xu, et al., Glucose oxidase driven hydrogen sulfide-releasing nanocascade for diabetic infection treatment, Nano Lett. 23 (14) (2023) 6610–6618.
[27] L. Chen, M. Peng, J. Zhou, X. Hu, Y. Piao, H. Li, et al., Supramolecular photothermal cascade nano-reactor enables photothermal effect, cascade reaction, and in situ hydrogelation for biofilm-associated tooth-extraction wound healing, Adv. Mater. 35 (31) (2023) e2301664.
[28] J. Cen, X. Dai, H. Zhao, X. Li, X. Hu, J. Wu, et al., Doxorubicin-loaded liposome with the function of "killing two birds with one stone" against glioma, ACS Appl. Mater. Interfaces 15 (40) (2023) 46697–46709.
[29] H.L. Xu, J.J. Yang, D.L. ZhuGe, M.T. Lin, Q.Y. Zhu, B.H. Jin, et al., Glioma-targeted delivery of a theranostic liposome integrated with quantum dots,

superparamagnetic iron oxide, and cilengitide for dual-imaging guiding cancer surgery, Adv. Healthcare Mater. 7 (9) (2018) e1701130.
[30] S. Joshi, J.R. Cooke, D.K. Chan, J.A. Ellis, S.S. Hossain, R.P. Singh-Moon, et al., Liposome size and charge optimization for intraarterial delivery to gliomas, Drug delivery and translational research 6 (3) (2016) 225–233.
[31] T. Wang, H. Zhang, H. Liu, Q. Yuan, F. Ren, Y. Han, et al., Boosting H2O2-guided chemodynamic therapy of cancer by enhancing reaction kinetics through versatile biomimetic Fenton nanocatalysts and the second near-infrared light irradiation, Adv. Funct. Mater. 30 (3) (2020) 1906128.
[32] Y. Hong, W. Hou, D. Ou, M. Lin, M. Luo, Q. Wei, Liposome-coated nanoparticle triggers prostate cancer ferroptosis through synergetic chemodynamic-gas therapy††Electronic supplementary information (ESI) available. See, Nanoscale Adv. 6 (2) (2024) 524–533, https://doi.org/10.1039/d3na00877k.
[33] C. Huang, X. Lin, T. Lin, W. Lin, Z. Gong, Q. Zheng, et al., Multifunctional nanocomposites induce mitochondrial dysfunction and glucose deprivation to boost immunogenic ferroptosis for cancer therapy, Chem. Eng. J. 466 (2023) 143012.
[34] J. Yang, B. Ren, H. Cai, W. Xiong, J. Feng, Q. Fan, et al., Cyclic catalysis of intratumor Fe(3+/2+) initiated by a hollow mesoporous iron sesquioxide nanoparticle for ferroptosis therapy of large tumors, Biomaterials 313 (2025) 122793.
[35] M. Ying, C. Zhan, S. Wang, B. Yao, X. Hu, X. Song, et al., Liposome-based systemic glioma-targeted drug delivery enabled by all-d peptides, ACS Appl. Mater. Interfaces 8 (44) (2016) 29977–29985.
[36] T.K. Shaw, P. Paul, Recent approaches and success of liposome-based nano drug carriers for the treatment of brain tumor, Curr. Drug Deliv. 19 (8) (2022) 815–829.
[37] Y. Rao, T. Fan, L. Zhou, K. Fang, Y. Sun, X. Hu, et al., A positive self-amplified H(2)O(2) and acidity circulation for boosting CDT-PTT-starvation therapy, J. Contr. Release : official journal of the Controlled Release Society 354 (2023) 701–712.
[38] Y. Liu, K. Chen, Y. Yang, P. Shi, Glucose oxidase-modified metal-organic framework for starving-enhanced chemodynamic therapy, ACS Appl. Bio Mater. 6 (2) (2023) 857–864.
[39] Y. Zong, H. Li, P. Liao, L. Chen, Y. Pan, Y. Zheng, et al., Mitochondrial dysfunction: mechanisms and advances in therapy, Signal Transduct. Targeted Ther. 9 (1) (2024) 124.
[40] J. Lu, L. Song, S. Feng, K. Wang, Y. Mao, Y. Gao, et al., Nanozyme-mediated biocatalysis as a mitochondrial oxidative stress amplifier for tumor nanocatalytic immunotherapy, Chem. Eng. J. 481 (2024) 148270.
[41] Y. Du, R. Zhang, J. Yang, S. Liu, J. Zhou, R. Zhao, et al., A “closed-loop” therapeutic strategy based on mutually reinforced ferroptosis and immunotherapy, Adv. Funct. Mater. 32 (13) (2022) 2111784.
[42] W. Lu, W. Wang, Y. Gong, J. Li, Y. Zhou, Y. Yang, A noncationic biocatalytic nanobiohybrid platform for cytosolic protein delivery through controlled perturbation of intracellular redox homeostasis, Small (2024) e2407676.
[43] H. Liang, X. Wu, G. Zhao, K. Feng, K. Ni, X. Sun, Renal clearable ultrasmall single-crystal Fe nanoparticles for highly selective and effective ferroptosis therapy and immunotherapy, J. Am. Chem. Soc. 143 (38) (2021) 15812–15823.
[44] W. Deng, H. Shang, Y. Tong, X. Liu, Q. Huang, Y. He, et al., The application of nanoparticles-based ferroptosis, pyroptosis and autophagy in cancer immunotherapy, J. Nanobiotechnol. 22 (1) (2024) 97.
[45] F. Zhou, B. Feng, H. Yu, D. Wang, T. Wang, Y. Ma, et al., Tumor microenvironment-activatable prodrug vesicles for nanoenabled cancer chemoimmunotherapy combining immunogenic cell death induction and CD47 blockade, Adv. Mater. 31 (14) (2019) e1805888.
[46] Y. Wang, F. Gong, Z. Han, H. Lei, Y. Zhou, S. Cheng, et al., Oxygen-deficient molybdenum oxide nanosensitizers for ultrasound-enhanced cancer metalloimmunotherapy, Angew. Chem. 62 (9) (2023) e202215467.